


Cite this: *Analyst*, 2023, **148**, 6036

AQAFI: a bioanalytical method for automated KPIs quantification of fluorescent images of human leukocytes and micro–nano particles†

Muhammad A. Sami, ^{‡a} Muhammad Nabeel Tahir ^{‡a} and Umer Hassan ^{*a,b}

Micro–nanoparticle and leukocyte imaging find significant applications in the areas of infectious disease diagnostics, cellular therapeutics, and biomanufacturing. Portable fluorescence microscopes have been developed for these measurements, however, quantitative assessment of the quality of images (micro–nanoparticles, and leukocytes) captured using these devices remains a challenge. Here, we present a novel method for automated quality assessment of fluorescent images (AQAFI) captured using smartphone fluorescence microscopes (SFM). AQAFI utilizes novel feature extraction methods to identify and measure multiple features of interest in leukocyte and micro–nanoparticle images. For validation of AQAFI, fluorescent particles of different diameters (8.3, 2, 1, 0.8 μm) were imaged using custom-designed SFM at a range of excitation voltages (3.8–4.5 V). Particle intensity, particle vicinity intensity, and image background noise were chosen as analytical parameters of interest and measured by the AQAFI algorithm. A control method was developed by manual calculation of these parameters using ImageJ which was subsequently used to validate the performance of the AQAFI method. For micro–nanoparticle images, correlation coefficients with $R^2 > 0.95$ were obtained for each parameter of interest while comparing AQAFI vs. control (ImageJ). Subsequently, key performance indicators (KPIs) *i.e.*, signal difference to noise ratio (SDNR) and contrast to noise ratio (CNR) were defined and calculated for these micro–nano particle images using both AQAFI and control methods. Finally, we tested the performance of the AQAFI method on the fluorescent images of human peripheral blood leukocytes captured using our custom SFM. Correlation coefficients of $R^2 = 0.99$ were obtained for each parameter of interest (leukocyte intensity, vicinity intensity, background noise) calculated using AQAFI and control (ImageJ). A high correlation was also found between the CNR and SDNR values calculated using both methods. The developed AQAFI method thus presents an automated and precise way to quantify and assess the quality of fluorescent images (micro–nano particles and leukocytes) captured using portable SFMs. Similarly, this study finds broader applicability and can also be employed with benchtop microscopes for the quantitative assessment of their imaging performance.

Received 10th July 2023,
Accepted 23rd October 2023
DOI: 10.1039/d3an01166f
rsc.li/analyst

1. Introduction

Fluorescence microscopy has been established as one of the most fundamental methods used by modern-day researchers.^{1,2} This fundamental investigative technique is not limited to a single branch of science but finds utility in a multitude of scientific and research settings involving the fields of

biology, environmental monitoring, material, and health sciences.^{3–5} Furthermore, continued advances in the fields of fluorophore design, molecular biological tools, and advancement in the optical resolution of these instruments are poised to dramatically revolutionize the future of research and human knowledge.^{1–5} Though fiercely efficient and robust, there are many factors *e.g.* high cost, the requirement of a trained technician, and the inability to work at the point of care (POC) settings that limit the effectiveness of fluorescence microscopes.

Recently, smartphone fluorescence microscopes (SFMs) are becoming more popular because they offer similar functionalities offered by their benchtop counterparts at very low cost.^{6,7} According to the latest estimates, nearly one-third of the world's population now have access to smartphones, surpassing the number of digital camera users, while digital camera sales continue to decline even further.⁸ Furthermore, smart-

^aDepartment of Electrical and Computer Engineering at Rutgers, The State University of New Jersey, New Brunswick, USA. E-mail: umer.hassan@rutgers.edu;

Tel: +1 (848) 445-2164

^bGlobal Health Institute at Rutgers, The State University of New Jersey, New Brunswick, USA

†Electronic supplementary information (ESI) available: Supplementary figures and tables. See DOI: <https://doi.org/10.1039/d3an01166f>

‡These authors contributed equally to the work.

phone fluorescence microscopes (SFM) are ideal devices to fulfill the growing need for point-of-care (POC) devices because of their robustness, convenience, portability, and low cost.⁹

In the past, researchers have shown the utility of SFMs in a multitude of applications ranging from biological to environmental settings.⁹ The authors in ref. 10 showcased an SFM with a limit of detection of 1 nM for on-site measurement and quantification of Hg²⁺ pollutants. Similarly, in ref. 11, the authors introduced an alternative design of SFM that focuses on detecting the norovirus in water samples at a single virus level. Similarly, in ref. 12, researchers have presented another design of SFM that aims at the detection of *Trypanosoma cruzi* parasites, which are responsible for an infectious disease called the Chagas. The study presented in ref. 13 developed a high-quality multichannel fluorescence microscope by using the Microscopy with Ultraviolet Surface Excitation (MUSE) technique and demonstrated the sub-micron resolution. Furthermore,¹⁴ discusses the working of another SFM for the imaging and detection of fluorescently labeled bacterial samples. Another study¹⁵ presented a technique that combined quantum dot barcode technology with smartphones and used them to detect HIV and Hepatitis B viruses. Additionally, in ref. 16, researchers developed an SFM to image and estimate the size of single DNA molecules. Another microfluidic biosensor utilized an SFM and employed fluorescence labeling and video processing techniques for real-time detection of *Salmonella typhimurium*.¹⁷ Furthermore, researchers in ref. 18 discussed the design and working of a smartphone microscope with multi-color fluorescence and a single contact lens-like add-on lens. This SFM had a slide launched total internal reflection guided illumination and could be used for studies involving autofluorescence, fluorescent stains, and immunofluorescence.¹⁸

Previously, our group has been involved in research focusing on designing multiple smartphone fluorescence microscopes.^{19–21} The initial version of our SFM design was capable of working with multiple fluorophores, offered compatibility with multiple modern smartphones, and just like its benchtop counterparts, offered the user multiple magnification levels.²⁰ Furthermore, in order to automate the counting of particles imaged using our SFM, we also worked on the development of a particle quantification algorithm using deep convolutional neural networks.^{22,23} Afterward, we improved the performance of our SFM by imaging fluorescent nanoparticles. This was done by enhancing the optics involved in the SFM and by studying the effect of different excitation modalities on the imaging performance of different SFM design variants.²¹ It was at this point that we realized that in addition to imaging smaller and smaller fluorescent particles, we also need a metric to quantifiably assess the quality of the fluorescent images captured using a particular SFM design.²¹ To do so, we picked two success metrics, the signal difference to noise ratio (SDNR) and contrast to noise ratio (CNR).^{24–27} These metrics are calculated on the basis of bead intensity, bead vicinity intensity, and the background noise in the cap-

tured image as shown in Fig. 1. We then quantified the imaging performance of the SFM design variants on the basis of these two parameters and found the best performing design.²¹ The SDNR and CNR parameters for a fluorescent image captured using SFM were calculated manually by using ImageJ. Though this manual processing gave us a reasonably good estimate of the performance of different SFM variants, it is a very resource and time-intensive method and also only considers a portion of the captured images for SDNR and CNR calculations.

In this paper, we have developed an algorithm for Automated Quality Assessment for Fluorescent Images (AQAFI).²⁸ AQAFI can be used for quantitatively assessing the quality of fluorescent images captured using an SFM. Green-fluorescent beads of four different sizes (8.3, 2, 1, 0.8 μm) were imaged at a range of excitation voltages (3.8–4.5 V) using an SFM that was previously designed by our group.²¹ These fluorescent micro-nano particles were carefully chosen to mimic the properties of a range of biological specimens such as leukocytes and bacterial cells. Additionally, many biological protocols such as phagocytic activity monitoring and cellular tracking directly rely on using fluorescent micro-nano particles.²⁹ Thus, these micro-nano particles were imaged using the designed SFM to validate its performance. Both ImageJ and the developed algorithm were used to quantify mean bead intensity, mean bead vicinity intensity, and the background noise in these captured images. Afterward, we calculated the SDNR and CNR values from the bead images captured in their respective optimal excitation region using the data obtained from both ImageJ and the automated algorithm. Next, we applied the developed algorithm to the images of fluorescent peripheral blood leukocytes captured using the SFM and quantified their SDNR and CNR values. Comparative analyses were also done on the results that were obtained using ImageJ and the automated algorithm. The designed automated algorithm can be used for robust and precise quantitative assessment of the quality of fluorescent images captured using SFM designs.

2. Materials and methods

2.1. Smartphone fluorescence microscope

The CAD model for the smartphone-based fluorescence microscope (SFM) is shown in Fig. 1A. The SFM is comprised of two main parts: the top part and the bottom part. The top portion houses slots for a 3.1 mm focal length lens from Edmund optics (Stock #87-165) and a long pass filter with a cut-off value of 500 nm (Semrock, Product no: FF01-500/LP-23.3-D). The lens is used for the magnification while the filter aids in generating the required darkfield for fluorescence microscopy. Additionally, the four screws slots in the top portion can be used for further tuning of SFM in the manual z-stage. The bottom portion of the SFM primarily consists of two cavities. One cavity is used for housing the batteries while the other cavity is intended for holding specimens under examination. The bottom portion also accommodates a laser module that

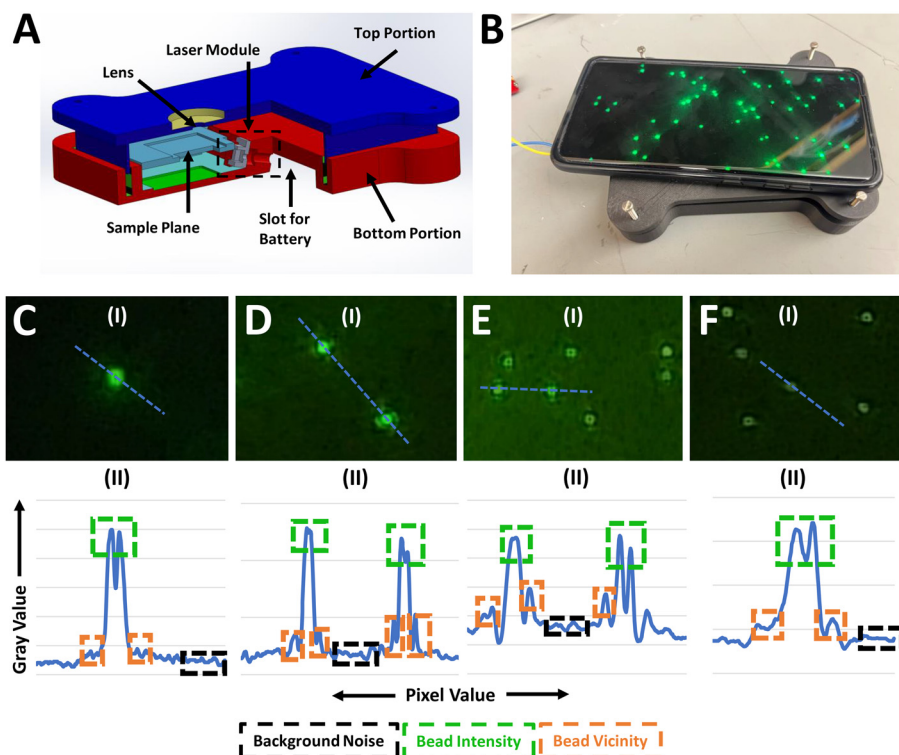


Fig. 1 (A) The CAD 3D design of the SFM. (B) The 3D printed experimental setup and prototype of SFM with a Samsung Galaxy S21 Ultra. (C)(I) The fluorescence image of 8.3 μm bead captured with designed SFM at 3.8 V. (II) The intensity plot of the 8.3 μm bead pixels obtained using ImageJ. (D)(I) The fluorescence image of 2 μm bead captured with designed SFM at 4.4 V. (II) The intensity plot of the 2 μm bead pixels obtained using ImageJ. (E)(I) The fluorescence image of 1 μm bead captured with designed SFM at 4.5 V. (II) The intensity plot of the 1 μm bead pixels obtained using ImageJ. (F)(I) The fluorescence image of 1 μm bead captured with designed SFM at 4.5 V. (II) The intensity plot of the 0.8 μm bead pixels obtained using ImageJ.

has been used as an excitation source. The laser module includes a 10 mm focal length lens (Edmund optics, Stock #45-208) and a 450 nm laser diode. To prevent the unwanted wavelengths from reaching the experiment plane a bandpass optical filter with a center wavelength of 470 nm (Chroma Inc., Product no. ET470/40x) and bandwidth of 40 nm is positioned in front of the laser diode. The designed SFM was 3D printed using Mark II 3D printer from Markforged using onyx thermoplastic material. The resulting 3D-printed SFM prototype was used alongside a Samsung Galaxy S21 Ultra for capturing images as shown in Fig. 1B. A DC power supply (EVENTEK, KPS3010D) was used to power the excitation source in order to minimize fluctuations. To evaluate the performance of the designed SFM against the excitation voltages the fluorescent beads were imaged in a voltage range of 3.8 V to 4.5 V, with a step size of 0.1 V.

2.2. Fluorescent bead sample preparation

The designed SFM was used to image green-fluorescent beads of four distinct sizes: (8.3, 2, 1, and 0.8 μm). The fluorescent beads 8.3 μm (Product #UMDG003), 2.0 μm (Product #FSDG005), and 1.0 μm (Product #FSDG004) were procured from Bandlaboratories, while the 0.8 μm beads were procured from SpheroTech (product number: HFP-0852-5). Various concentrations of these beads were prepared using 1 \times PBS solution. A

1 μL sample of each bead size (8.3, 2, 1, 0.8 μm) was imaged at voltage values ranging from 3.8 to 4.5 V using the designed SFM.

2.3. Fluorescent bead optimal excitation voltage range

The SFM imaged each fluorescent bead sample at excitation voltage values ranging from 3.8 to 4.5 V. By juxtaposing these obtained images, we identified three separate regions within the excitation voltage range. The lower excitation voltages that are not able to fully capture the beads result in the data loss region. The higher excitation voltages result in a region called the high noise region, which contains all the fluorescent beads along with the high image noise. Sandwiched between these two regions is the optimal excitation voltage region, where neither data loss nor excessive noise occurred, and the image quality was deemed acceptable. To provide a comprehensive overview, the optimal excitation voltage ranges for all four bead sizes (8.3, 2, 1, and 0.8 μm) are presented in ESI Table S1.† A detailed protocol outlining the methodology employed to identify these optimal ranges can be found in our previous study.²¹

2.4. Fluorescent bead image acquisition protocol

To ensure consistency throughout the study, all the images were captured using Samsung S21 Ultra at a digital zoom of 6 \times using auto-mode. The auto-mode helped the smartphone to

automatically select the imaging parameters *e.g.* focus, exposure time, and white balance. For each bead size (8.3, 2, 1, and 0.8 μm), a 1 μl sample was imaged using the designed SFM at voltage values ranging from 3.8 V to 4.5 V, with a step size of 0.1 V. To account for experimental variations, three samples from each bead size were imaged within the voltage range of 3.8 V to 4.5 V.

2.5. Image quality assessment using ImageJ

Following the imaging of the four bead sizes (8.3, 2, 1, and 0.8 μm) using the SFM, a comprehensive analysis was conducted to evaluate the SFM's imaging performance. Fig. 1C–F displays representative images captured for the 8.3 μm , 2.0 μm , 1.0 μm , and 0.8 μm beads. ImageJ was utilized to measure the bead intensity, vicinity intensity, and background noise profiles for each image. Based on these three parameters, the signal difference to noise ratio (SDNR) and contrast to noise ratio (CNR) was calculated for individual beads present in the captured images, using the respective eqn (1), (2), and (3).^{24–27}

$$\text{SDNR} = \frac{\text{Bead Intensity} - \text{Vicinity Intensity}}{\text{Background Noise}} \quad (1)$$

$$\text{Contrast} = \frac{\text{Bead Intensity} - \text{Vicinity Intensity}}{\text{Vicinity Intensity}} \quad (2)$$

$$\text{CNR} = \frac{\text{Contrast}}{\text{Background Noise}} \quad (3)$$

To determine the SDNR and CNR values for a complete image, the average SDNR and CNR values of ten beads within that image were calculated. The selection of these ten beads followed a specific methodology. The image was divided into

three distinct regions, and a diagonal line was drawn from the bottom left corner to the top right corner, as illustrated in ESI Fig. S1.† For analysis purposes, the beads closer to the diagonal line were picked, the three beads were selected from both Regions 1 and 3, while four beads were selected from Region 2. In cases where a region contained fewer than the required number of beads, additional beads from other regions were selected to ensure a total of ten beads for analysis. It is important to note that the bead intensity, vicinity intensity, and background noise parameters were measured for images of all four bead sizes (8.3, 2, 1, and 0.8 μm) at each excitation voltage ranging from 3.8 V to 4.5 V. However, the SDNR and CNR parameters were specifically calculated for each bead size based on its respective optimal excitation voltage range.

2.6. Image quality assessment using AQAFI

AQAFI was built upon existing state-of-the-art image processing-based feature extraction methods. The algorithm automates the process for the calculation of bead intensity, vicinity intensity, and background noise of each captured fluorescent bead image. Fig. 2 showcases the flowchart and steps taken by the algorithm for the estimation of the previously stated parameters.

2.6.1. Image representation. The image obtained by an SFM can be represented mathematically as in eqn (4).

$$\tilde{\mathbf{I}}(\mathbf{x}, \mathbf{y}) = \mathbf{I}(\mathbf{x}, \mathbf{y}) + \mathbf{n}(\mathbf{x}, \mathbf{y}) + \sum_{i=1}^K g(ax - x_i, ay - y_i, \mathcal{J}_i, \mathcal{J}_i^v) \quad (4)$$

Here $\mathbf{I}(\mathbf{x}, \mathbf{y})$ in the equation is the base image while $\tilde{\mathbf{I}}(\mathbf{x}, \mathbf{y})$ represents an image that contains the K beads, the original image, and background noise. The function $g(\cdot)$ represents a

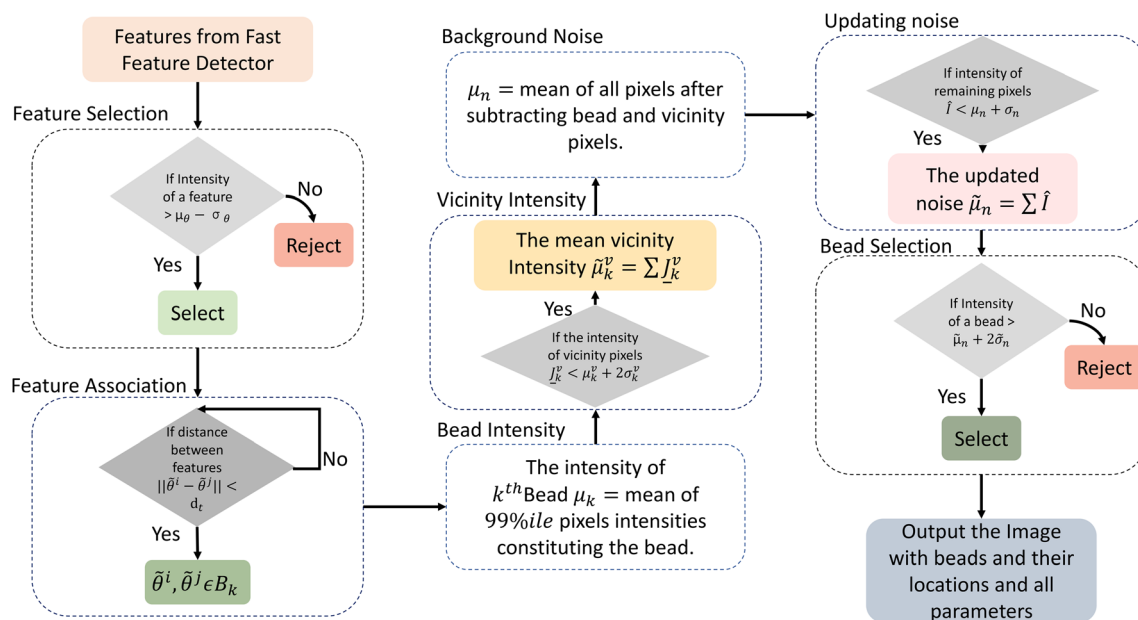


Fig. 2 Flow chart depicting the process flow of the designed automated algorithm for quantitative assessment of the quality of fluorescent images captured using smartphone fluorescence microscopes.

bead of size α , located at (x_i, y_i) and is summed for K beads in the image, and $\mathbf{n}(\mathbf{x}, \mathbf{y})$ is the background noise. The parameters in $g(\cdot)$ represent the location, bead intensity, and vicinity intensity of a particular bead. We assume that the bead intensity \mathcal{J}_i , vicinity intensity \mathcal{J}_i^v , and background noise can be considered as Gaussian distributions with means and standard deviations $\mu_{\mathcal{J}}, \sigma_{\mathcal{J}}, \mu_{\mathcal{J}^v}, \sigma_{\mathcal{J}^v}$, and μ_n, σ_n respectively as shown in eqn (5), (6), and (7).

$$\mathcal{J}_i = \mathcal{N}(\mu_{\mathcal{J}}, \sigma_{\mathcal{J}}) \quad (5)$$

$$\mathcal{J}_i^v = \mathcal{N}(\mu_{\mathcal{J}^v}, \sigma_{\mathcal{J}^v}) \quad (6)$$

$$n = \mathcal{N}(\mu_n, \sigma_n) \quad (7)$$

2.6.2. Feature detection. The algorithm detects features associated with each bead, using fast feature detection.³⁰ The algorithm performs basic mathematical operations on a given pixel \mathbf{p} located at (x, y) and finds if the pixel is a feature associated with a bead using the following steps:

S.1 First a target pixel \mathbf{p} is selected at the location (x, y) and a threshold ΔI for the intensity values is picked based on the bead of size α present in the image.

S.2 In the following step a Bresenham circle is selected of radius 3. The circle contains the 16 pixels around the target point \mathbf{p} .

S.3 Now the pixel \mathbf{p} will be considered as a potential feature or corner if there are P contiguous pixels in the Bresenham circle that are either darker than $\tilde{I}(x, y) - \Delta I$, or brighter than $\tilde{I}(x, y) + \Delta I$. A default value of $P = 12$ ³⁰ was used in this study.

S.4 A simple test on the selected pixel improves the overall computational cost of the algorithm. The intensity of the target pixel is compared with the intensities of the pixels at locations $\{1, 3, 5, 9, 13\}$. If at least three or the majority of these pixels satisfy the criterion as stated in the S.3, the target point is considered a feature, and all the pixels are tested. And if the pixels fail the test the pixel is rejected as a feature.

S.5 The steps S.1–S.4 are repeated for each pixel in the image.

After applying the above-stated algorithm on each pixel, we get a vector of features $\underline{\theta}$, where each $\theta^i \in \underline{\theta}$ is a pixel location in the image showcasing potential features as seen in ESI Fig. S24.[†]

2.6.3. Feature selection and association. We discard the low information features by selecting all the features that satisfy the condition:

$$\mathcal{J}(\theta^i) > \mu_{\theta} - \sigma_{\theta} \quad (8)$$

The function $\mathcal{J}(\theta^i)$ represents the intensity of the feature θ^i . Where μ_{θ} is the mean and σ_{θ} is the standard deviation all feature intensities. The resultant feature vector contains less or equal features as in $\underline{\theta}$ and can be represented as $\tilde{\underline{\theta}}$. Discarding the low information features reduces the possibility of a noise element being selected as a feature and introduces robustness in the algorithm. The features are associated with their respective beads by applying an approach similar to agglomerative clustering. This is done by calculating the Euclidean

distance of each feature from all other features and associating all the features to a particular bead that has a Euclidean distance less than a predefined distance threshold d_t . The final location of any particular bead is calculated as the center point of all the features associated with that particular bead and is explained in the eqn (9).

$$l_k = \frac{1}{S} \sum_{i=1}^S \tilde{\theta}_k^i \quad (9)$$

where l_k is location, while S is the number of features associated with k th bead.

2.6.4. Preliminary bead intensity. The bead intensity is calculated as the mean of all the pixel intensities which are above 99%ile in a square of size $4s^2$ around the k th bead as shown in eqn (10).

$$\mathcal{J}_k = \overline{99\%ile(\underline{\mathcal{J}}(l_k \pm s))} \quad (10)$$

where s is the half length of the square.

2.6.5. Preliminary vicinity noise. To calculate vicinity noise intensity we first remove all the pixels in a circular area equal to the size α of the bead and then take the mean of the remaining pixels as shown in ESI Fig. S3.[†] The eqn (11) and (12) show the process to estimate the vicinity intensity.

$$\underline{\mathcal{J}}_k^v = \underline{\mathcal{J}}(l_k \pm s) - \underline{\mathcal{J}}(l_k \pm \alpha) \quad (11)$$

$$\mu_k^v = \frac{1}{p} \sum_{i=1}^p (\underline{\mathcal{J}}_k^v) \quad (12)$$

where p represents the number of pixels constituting the vicinity region.

The vicinity noise for a particular bead is then updated by calculating the mean of all the pixels that have intensity values less than two standard deviations from the previous mean. The eqn (13) provides the mathematical representation of the updated vicinity intensity mean $\tilde{\mu}_k^v$.

$$\tilde{\mu}_k^v = \frac{1}{m} \sum_{k=1}^m \mathcal{J}_k^v \left(1_{\underline{\mathcal{J}}_k^v < \mu_k^v + 2 \times \sigma_k^v}(\underline{\mathcal{J}}_k^v) \right) \quad (13)$$

where σ_k^v is the standard deviation of the vicinity noise pixels for k th bead. The $1(\cdot)$ is the indicator function and is represented as:

$$1_A(x) := \begin{cases} 1 & \text{if } x \in A \\ 0 & \text{if } x \notin A \end{cases} \quad (14)$$

Thus by using the indicator function, we select only those pixels that satisfy the condition $\underline{\mathcal{J}}_k^v < \mu_k^v + 2 \times \sigma_k^v$. The update step reduces the chances of residual bead pixels being incorporated while calculating the vicinity noise intensity. As the bead pixels have a higher intensity than the vicinity noise pixels the update step discards these outliers and improves the accuracy of the calculated vicinity noise.

2.6.6. Background noise. As the location of all the detected beads and the vicinity intensity is updated we remove all the pixels that belong to either bead or vicinity noise, by setting

these pixel intensities to zero as shown in ESI Fig. S4.† The resulting image can be mathematically represented in eqn (15).

$$\hat{\mathbf{I}}(\mathbf{x}, \mathbf{y}) = \tilde{\mathbf{I}}(\mathbf{x}, \mathbf{y}) - \sum_1^K \mathcal{J}(l_k \pm s) \quad (15)$$

The background noise is calculated by calculating the mean of all the pixel intensities in the image $\tilde{\mathbf{I}}(\mathbf{x}, \mathbf{y})$ as shown in the eqn (16).

$$\mu_n = \frac{1}{N} \sum_{i=1}^N (\hat{I}(x_i, y_i)) \quad (16)$$

To accurately estimate the background noise and minimize the possibility of selecting the pixels associated with the undetected beads as shown in Fig. S4,† the background noise is updated in a similar fashion to the vicinity intensity and this process can be modeled by using the eqn (17).

$$\tilde{\mu}_n = \frac{1}{M} \sum_1^M \hat{I}(1_{\hat{I} < \mu_n + \sigma_n}(\hat{I})) \quad (17)$$

Here the σ_n is the standard deviation of all the pixel intensities in the background noise.

2.6.7. Final bead and vicinity intensity (extirpating false positives). Finally, to improve the number of beads detected and decrease the probability of selecting a false feature as a bead we employ a bead selection strategy at the final stage of our algorithm. The beads which have a mean intensity greater than the two standard deviations of background noise are selected and the rest are removed. The mathematical representation is shown in eqn (18).

$$\tilde{\underline{\mathbf{B}}} = \underline{\mathbf{B}}(1_{\mathcal{J} > \tilde{\mu}_n + 2 \times \tilde{\sigma}_n}(\underline{\mathcal{J}})) \quad (18)$$

The overall mean bead intensity and the associated vicinity noise in the entire image are calculated by taking the average of all the bead and vicinity noise intensities in $\tilde{\underline{\mathbf{B}}}$. The resulting algorithm (AQAFI) for quantitative quality assessment of fluorescent images captured using an SFM is presented in Algorithm 1 and the different input metrics used by the algorithm are shown in ESI Table S2.†

Algorithm 1 AQAFI

Require d_t = distance threshold

Require s = half length of square space around bead.

Require α = bead size

Given an Image $\tilde{\mathbf{I}}(\mathbf{x}, \mathbf{y})$ as in (4) get features $\underline{\mathcal{Q}}$ using 2–2.

Select the features if.

for each $\theta^i \in \underline{\mathcal{Q}}$ **do**

if $\mathcal{J}(\theta^i) > \mu_\theta - \sigma_\theta$ then

Select the feature θ^i .

else if $\mathcal{J}(\theta^i) < \mu_\theta - \sigma_\theta$ then

Reject the feature θ^i .

end if

end for

Return updated features $\tilde{\underline{\mathcal{Q}}}$.

for each θ^i and $\theta^j \in \tilde{\underline{\mathcal{Q}}}$ **do**

if $||\theta^i - \theta^j|| < d_t$ then

$\theta^i, \theta^j \in B_k$ and

Calculate bead location l_k using (9).

Calculate bead intensity \mathcal{J}_k using (10).

Remove bead intensity features using (11).
Calculate mean vicinity intensity μ_k^v by (12).
Update mean vicinity intensity $\tilde{\mu}_k^v$ with (13).
Remove vicinity intensity pixels using (11) and calculate background noise mean μ_n with (16).
Update background noise $\tilde{\mu}_n$ with (17).
Update detected beads $\underline{\mathbf{B}}$ by using (18).

end if
end for

2.7. Leukocyte imaging and quality assessment

In addition to the fluorescent beads, the applicability of the designed algorithm was also tested on human peripheral blood leukocytes. To do so, the blood samples were obtained from Robert Wood Johnson Hospital (RWJH) in New Jersey following the approved guidelines of the Institutional Review Board (IRB) at Rutgers University (IRB application: Pro2018002356). To isolate Leukocytes from the whole blood the red blood cells were initially using RBC lysis media from ThermoFisher (Cat: 00-4333-57). 100 μ l of whole blood and 1 ml of lysis media were incubated at room temperature for 10 minutes. The lysis process was halted by adding 2 ml of 1 \times PBS to the mixture. Subsequently, the blood samples were centrifuged at 500g for 5 minutes, and the supernatant was discarded to obtain the leukocyte pellet. These leukocytes were then resuspended in 1 ml of 1 \times PBS solution. To fluorescently label the leukocyte samples, SYTO 16 nuclear stain from ThermoFisher (Catalogue: S7578) was employed. The nuclear stain and the leukocyte sample were added in a 1 : 1 ratio and incubated in the dark for 15 minutes at room temperature. These fluorescent leukocytes were then imaged using the smartphone fluorescence microscope at multiple voltage levels ranging from 4.0 to 4.5 V.

A protocol similar to fluorescent bead imaging was used for imaging fluorescently tagged peripheral blood leukocytes. 1 μ l drop of leukocyte sample was imaged at voltage values ranging from 4.0 to 4.5 V with a step size of 0.1 V using the designed SFM and Samsung Galaxy S21 Ultra. The leukocyte imaging experiments were also done in triplicates to account for the variance between experiments. To quantify the quality of the leukocyte fluorescent images, the SDNR and CNR parameters are calculated for the imaged leukocytes (4.0–4.5 V) based on eqn (1), (2), and (3) using both AQAFI and the previously described manual method using ImageJ. The terms bead intensity and bead vicinity noise in the algorithm and the equations above refer to leukocyte intensity and leukocyte vicinity noise while analyzing leukocyte images.

3. Results

3.1. Smartphone fluorescence microscope

The SFM was used in conjunction with a Samsung Galaxy S21 Ultra as shown in Fig. 1B. The camera module of the Samsung Galaxy S21 Ultra has an internal lens with a focal length of 6.7 mm which forms a relay lens with a 3.1 mm focal length external lens. The magnification factor produced by the combi-

nation of these lenses is equal to 2.16. As evident from Fig. 1C–F, the SFM was able to successfully image all four sizes (8.3, 2, 1, 0.8 μm) of the green-fluorescent beads.

3.2. Performance of AQAFI on fluorescent beads

As mentioned in the previous section, AQAFI assesses the quality of a captured image by calculating the bead intensity, bead vicinity intensity, and the background noise of an image. The results obtained using AQAFI for each of these parameters when compared to the ImageJ control are showcased in individual sections below:

3.2.1. Bead intensity. The SFM was used to image all four bead sizes (8.3, 2, 1, 0.8 μm) at multiple excitation voltages ranging from 3.8 to 4.5 V. The algorithm was then used to find the average bead intensity for each captured image and the obtained values were compared with control values obtained using ImageJ. Fig. 3A(I) shows the correlation curve between ImageJ bead intensities and algorithm bead intensities for the 8.3 μm beads. It shows a correlation coefficient of 0.99. We also performed Bland–Altman analysis on this data as shown in Fig. 3A(II); it shows an average difference of 10.86 between the two methods with 36.4 and -14.7 as limits of agreement. Fig. 3B(I) shows the correlation curve between ImageJ bead intensities and algorithm bead intensities for the 2 μm beads. It shows a correlation coefficient of 0.98. We also performed Bland–Altman analysis on this data as shown in Fig. 3B(II); it shows an average difference of 2.88 between the two methods with 16.8 and -11.0 as limits of agreement. Fig. 3C(I) shows the correlation curve between ImageJ bead intensities and algorithm bead intensities for the 1 μm beads. It shows a correlation coefficient of 0.98. We also performed Bland–Altman analysis on this data as shown in Fig. 3C(II); it shows an

average difference of 1.28 between the two methods with 19.6 and -17.1 as limits of agreement. Fig. 3D(I) shows the correlation curve between ImageJ bead intensities and algorithm bead intensities for the 0.8 μm beads. It shows a correlation coefficient of 0.98. We also performed Bland–Altman analysis on this data as shown in Fig. 3D(II); it shows an average difference of -0.7 between the two methods with 14.2 and -15.8 as limits of agreement.

3.2.2. Bead vicinity intensity. The SFM was used to image all four bead sizes (8.3, 2, 1, 0.8 μm) at multiple excitation voltages ranging from 3.8 to 4.5 V. The algorithm was then used to find the average bead vicinity intensity for each captured image and the obtained values were compared with control values obtained using ImageJ. Fig. 4A(I) shows the correlation curve between ImageJ bead vicinity intensities and algorithm bead vicinity intensities for the 8.3 μm beads. It shows a correlation coefficient of 0.97. We also performed Bland–Altman analysis on this data as shown in Fig. 4A(II); it shows an average difference of 10.74 between the two methods with 21.8 and -0.3 as limits of agreement. Fig. 4B(I) shows the correlation curve between ImageJ bead vicinity intensities and algorithm bead vicinity intensities for the 2 μm beads. It shows a correlation coefficient of 0.96. We also performed Bland–Altman analysis on this data as shown in Fig. 4B(II); it shows an average difference of 1.56 between the two methods with 7.7 and -4.6 as limits of agreement. Fig. 4C(I) shows the correlation curve between ImageJ bead vicinity intensities and algorithm bead vicinity intensities for the 1 μm beads. It shows a correlation coefficient of 0.98. We also performed Bland–Altman analysis on this data as shown in Fig. 4C(II); it shows an average difference of 0.45 between the two methods with 5.1 and -4.1 as limits of agreement. Fig. 4D(I) shows the

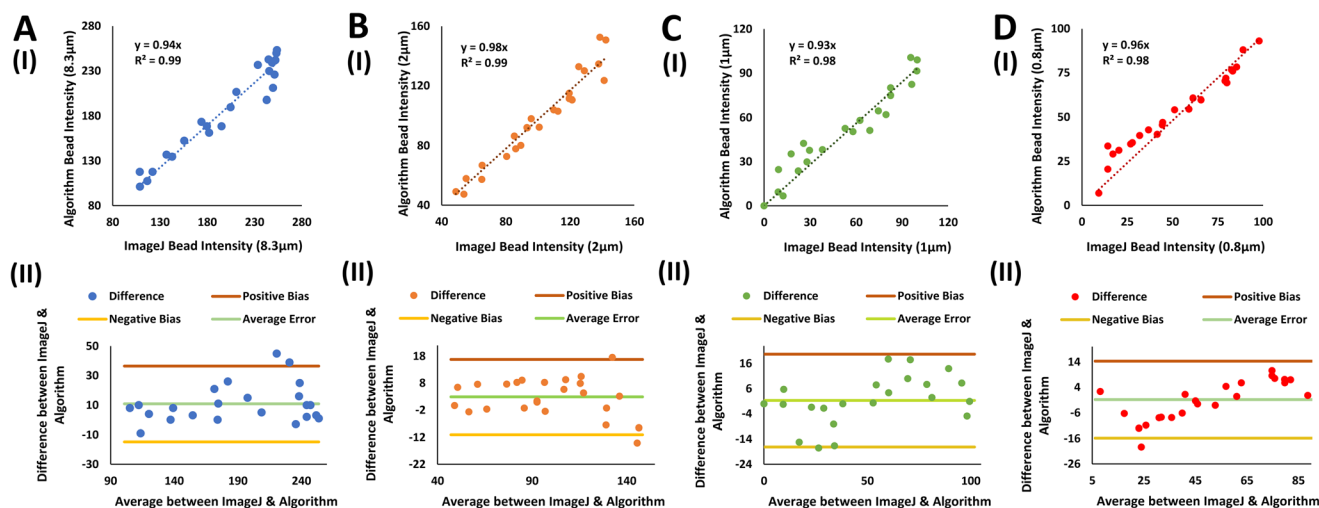


Fig. 3 (A)(I) The Correlation curve for bead intensities data collected using ImageJ and the proposed algorithm for the 8.3 μm beads. (II) The Bland–Altman analysis plots of the data presented in A(I). (B)(I) The Correlation curve for bead intensities data collected using ImageJ and the proposed algorithm for the 2 μm beads. (II) The Bland–Altman analysis plots of the data presented in B(I). (C)(I) The Correlation curve for bead intensities data collected using ImageJ and the proposed algorithm for the 1 μm beads. (II) The Bland–Altman analysis plots of the data presented in C(I). (D)(I) The Correlation curve for bead intensities data collected using ImageJ and the proposed algorithm for the 0.8 μm beads. (II) The Bland–Altman analysis plots of the data presented in D(I).

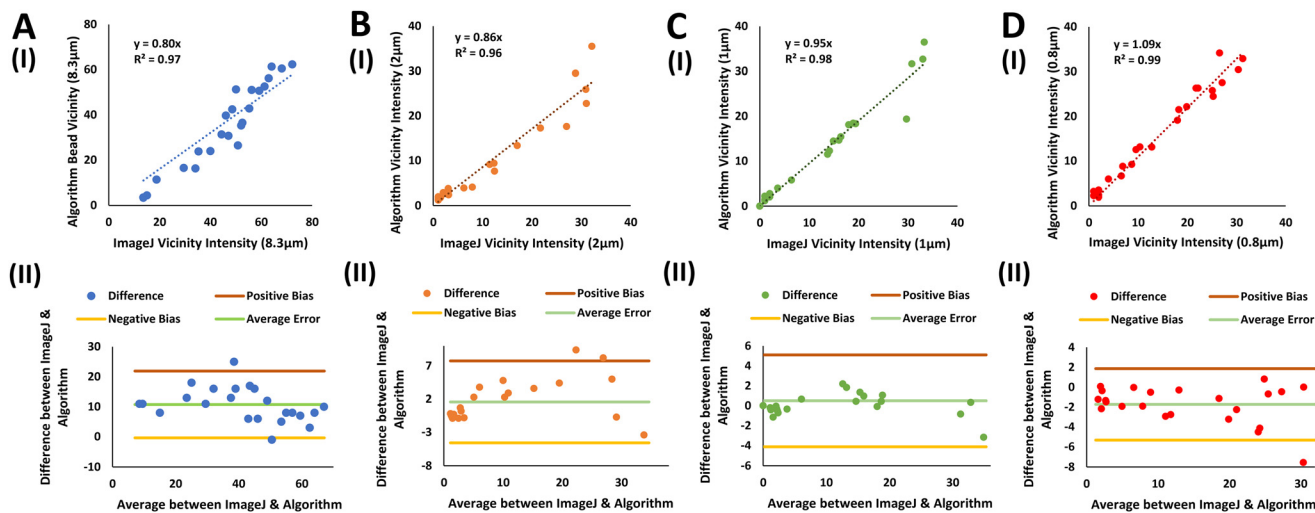


Fig. 4 (A)(I) The Correlation curve for bead vicinity intensities data collected using ImageJ and the proposed algorithm for the 8.3 μm beads. (II) The Bland–Altman analysis plots of the data presented in A(I). (B)(I) The Correlation curve for bead vicinity intensities data collected using ImageJ and the proposed algorithm for the 2 μm beads. (II) The Bland–Altman analysis plots of the data presented in B(I). (C)(I) The Correlation curve for bead vicinity intensities data collected using ImageJ and the proposed algorithm for the 1 μm beads. (II) The Bland–Altman analysis plots of the data presented in C(I). (D)(I) The Correlation curve for bead vicinity intensities data collected using ImageJ and the proposed algorithm for the 0.8 μm beads. (II) The Bland–Altman analysis plots of the data presented in D(I).

correlation curve between ImageJ bead vicinity intensities and algorithm bead vicinity intensities for the 0.8 μm beads. It shows a correlation coefficient of 0.99. We also performed Bland–Altman analysis on this data as shown in Fig. 4D(II); it shows an average difference of -1.74 between the two methods with 1.8 and -5.3 as limits of agreement.

3.2.3. Background noise. The SFM was used to image all four bead sizes (8.3, 2, 1, 0.8 μm) at multiple excitation vol-

tages ranging from 3.8 to 4.5 V. The algorithm was then used to find the background noise in each captured image and the obtained values were compared with control values obtained using ImageJ. Fig. 5A(I) shows the correlation curve between ImageJ background noise and algorithm background noise for the 8.3 μm beads. It shows a correlation coefficient of 0.97. We also performed Bland–Altman analysis on this data as shown in Fig. 5A(II); it shows an average difference of -1.2 between

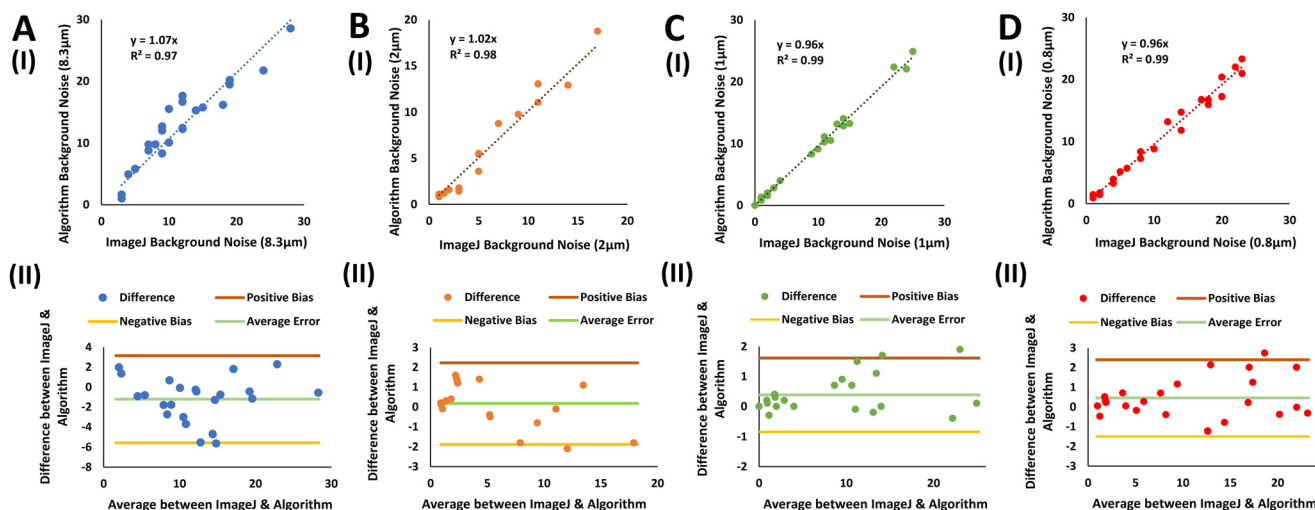


Fig. 5 (A)(I) The Correlation curve for the background noise data collected using ImageJ and the proposed algorithm for the 8.3 μm beads. (II) The Bland–Altman analysis plots of the data presented in A(I). (B)(I) The Correlation curve for the background noise data collected using ImageJ and the proposed algorithm for the 2 μm beads. (II) The Bland–Altman analysis plots of the data presented in B(I). (C)(I) The Correlation curve for the background noise data collected using ImageJ and the proposed algorithm for the 1 μm beads. (II) The Bland–Altman analysis plots of the data presented in C(I). (D)(I) The Correlation curve for the background noise data collected using ImageJ and the proposed algorithm for the 0.8 μm beads. (II) The Bland–Altman analysis plots of the data presented in D(I).

the two methods with 3.1 and -5.5 as limits of agreement. Fig. 5B(I) shows the correlation curve between ImageJ background noise and algorithm background noise for the $2\ \mu\text{m}$ beads. It shows a correlation coefficient of 0.98. We also performed Bland–Altman analysis on this data as shown in Fig. 5B(II); it shows an average difference of 0.18 between the two methods with 2.2 and -1.8 as limits of agreement. Fig. 5C(I) shows the correlation curve between ImageJ background noise and algorithm background noise for the $1\ \mu\text{m}$ beads. It shows a correlation coefficient of 0.99. We also performed Bland–Altman analysis on this data as shown in Fig. 5C(II); it shows an average difference of 0.38 between the two methods with 1.6 and -0.8 as the limits of agreement. Fig. 5D(I) shows the correlation curve between ImageJ background noise and algorithm background noise for the $0.8\ \mu\text{m}$ beads. It shows a correlation coefficient of 0.99. We also performed Bland–Altman analysis on this data as shown in Fig. 5D(II); it shows an average difference of 0.46 between the two methods with 2.4 and -1.4 as limits of agreement.

3.2.4. SDNR and CNR. The SFM was able to successfully image all four bead sizes (8.3 , 2 , 1 , $0.8\ \mu\text{m}$) as mentioned above. After measuring bead intensity, bead vicinity intensity, and background noise for each captured image using both the algorithm and ImageJ (control), we calculated SDNR and CNR values for each bead size in its respective optimal excitation range. For $8.3\ \mu\text{m}$ an optimal excitation voltage of $3.8\ \text{V}$ was identified. The SDNR values calculated using both the algorithm and ImageJ for $8.3\ \mu\text{m}$ beads imaged at the optimal excitation voltage are shown in Fig. 6A(I) and the corresponding CNR values are shown in Fig. 6A(II). For $2\ \mu\text{m}$ an optimal exci-

tation voltage of 4.1 to $4.3\ \text{V}$ was identified. The SDNR values calculated using both the algorithm and ImageJ for $2\ \mu\text{m}$ beads imaged at the optimal excitation voltage are shown in Fig. 6B(I) and the corresponding CNR values are shown in Fig. 6B(II). For $1\ \mu\text{m}$ an optimal excitation voltage of 4.3 to $4.5\ \text{V}$ was identified. The SDNR values calculated using both the algorithm and ImageJ for $1\ \mu\text{m}$ beads imaged at the optimal excitation voltage are shown in Fig. 6C(I) and the corresponding CNR values are shown in Fig. 6C(II). For $0.8\ \mu\text{m}$ an optimal excitation voltage of 4.3 to $4.5\ \text{V}$ was identified. The SDNR values calculated using both the algorithm and ImageJ for $0.8\ \mu\text{m}$ beads imaged at the optimal excitation voltage are shown in Fig. 6D(I) and the corresponding CNR values are shown in Fig. 6D(II).

3.3. Performance of AQAFI on leukocytes

The designed SFM was able to successfully image the fluorescent leukocytes as shown in Fig. 7. The images of the fluorescent leukocytes captured using the SFM were analyzed using both AQAFI and the ImageJ-based manual protocol. Fig. 7A(I) showcases the correlation plot between the leukocyte intensity values obtained using AQAFI and ImageJ and an R^2 value of 0.99 was obtained. The Bland Altman analysis of this data is shown in Fig. 7A(II) and a mean error of 6.73 with limits of agreement equal to 32.2 and -18.8 were obtained. Fig. 7B(I) showcases the correlation plot between the leukocyte vicinity intensity values obtained using AQAFI and ImageJ and an R^2 value of 0.99 was obtained. The Bland Altman analysis of this data is shown in Fig. 7B(II) and a mean error of 6.91 with limits of agreement equal to 12.6 and 1.1 was obtained.

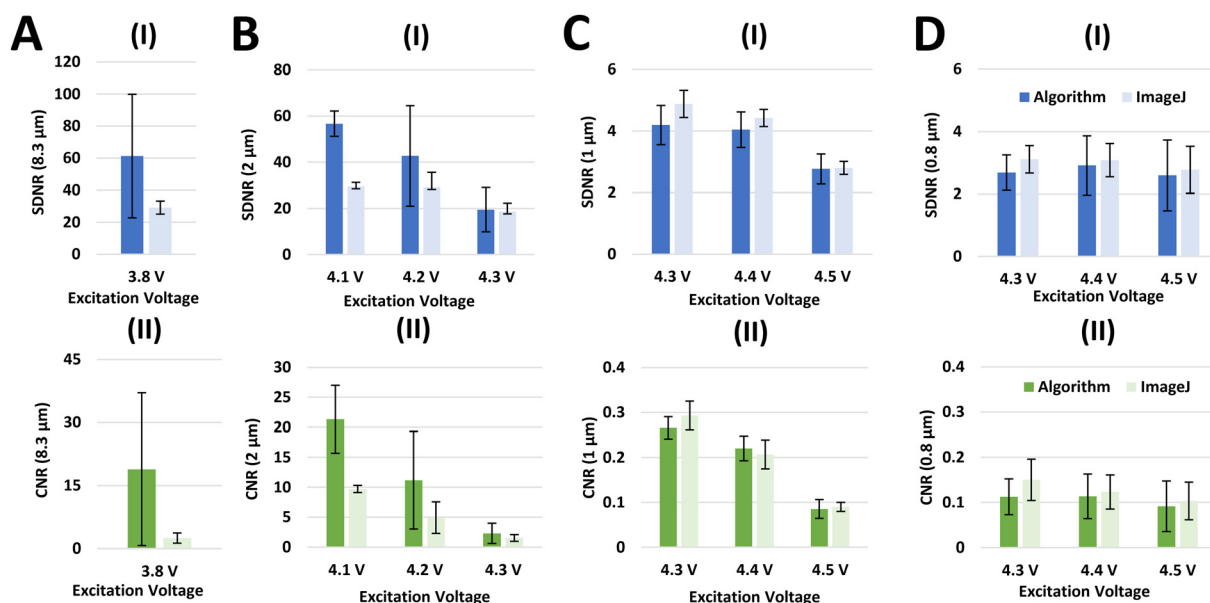


Fig. 6 (A)(I) SDNR values for $8.3\ \mu\text{m}$ beads calculated using both the proposed algorithm and ImageJ imaged at the optimal excitation voltage. (II) The Corresponding CNR values. (B)(I) SDNR values for $2\ \mu\text{m}$ beads calculated using both the proposed algorithm and ImageJ imaged at the optimal excitation voltage. (II) Corresponding CNR values. (C)(I) SDNR values for $1\ \mu\text{m}$ beads calculated using both the proposed algorithm and ImageJ imaged at the optimal excitation voltage. (II) The Corresponding CNR values. (D)(I) SDNR values for $0.8\ \mu\text{m}$ beads calculated using both the proposed algorithm and ImageJ imaged at the optimal excitation voltage. (II) The Corresponding CNR values.

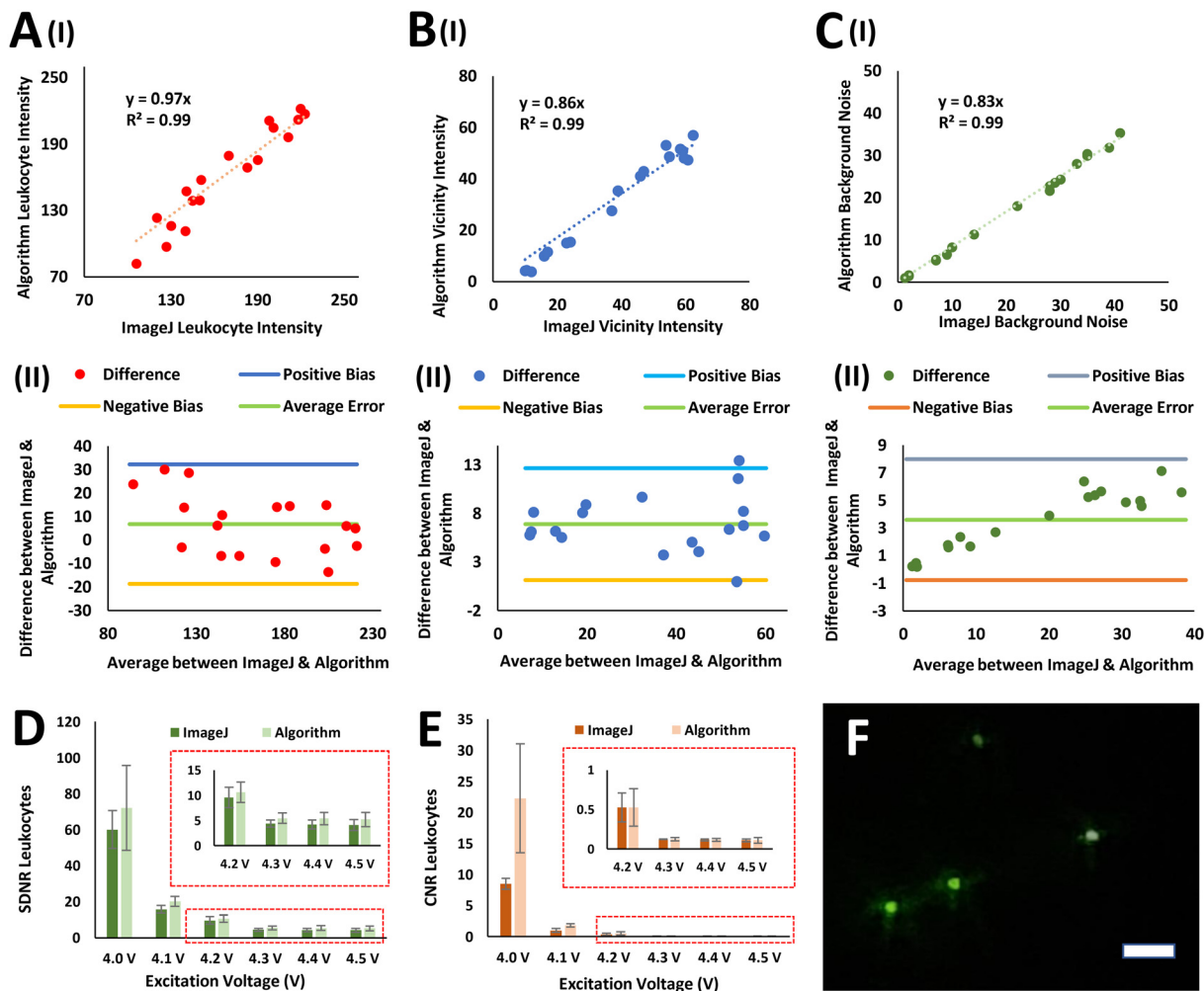


Fig. 7 (A)(I) Correlation plot between leukocyte intensity values obtained using algorithm and ImageJ. (A)(II) The Bland–Altman analysis plots of the data presented in (I). (B)(I) Correlation plot between leukocyte vicinity intensity values obtained using algorithm and ImageJ. (B)(II) The Bland–Altman analysis plots of the data presented in (I). (C)(I) Correlation plot between background noise values obtained using algorithm and ImageJ. (C)(II) The Bland–Altman analysis plots of the data presented in (I). (D) SDNR values of the leukocytes obtained using the algorithm and ImageJ. (E) CNR values of the leukocytes obtained using the algorithm and ImageJ. (F) Cropped leukocyte image obtained using the SFM at an excitation voltage of 4.0 V (scale bar = 30 μm).

Similarly, the correlation plot between the background noise values obtained using AQAFI and ImageJ is shown in Fig. 7C(I) and an R^2 value of 0.99 was obtained. The Bland Altman analysis of this data is shown in Fig. 7C(II) with a mean error equal to 3.5 and limits of agreement equal to 7.9 and -0.8 . Based on these parameters of interest, SDNR and CNR values were calculated, and they are shown in Fig. 7D and E respectively.

4. Discussion

Smartphone fluorescence microscopes (SFM) are becoming more and more popular as they offer some of the major functionalities offered by their benchtop counterparts at a fraction of the cost.^{6,7} A plethora of SFM designs have been showcased to date and they have been for all sorts of applications ranging

from environmental monitoring to healthcare testing.⁹ As shown in Fig. 1 the SFM discussed in this paper is capable of imaging a wide range of fluorescent specimens ranging from a few microns to sub-microns in size. The choice of smartphone and the external lens used for creating magnification immensely affect the SFM performance and in its current configuration, the presented SFM has a measured optical resolution of about 2.2 μm .²¹ Simply measuring the optical resolution alone is not enough, we need to have more quantifiable metrics to compare the final imaging performances of different SFM designs and configurations so that we can get a better understanding of their performance limitations and work toward improving them.

In order to quantify the quality of an image captured using the SFM, we chose two performance metrics, the contrast to noise ratio (CNR) and the signal difference to noise ratio (SDNR).^{24–27} Contrast is directly related to the ability to differ-

entiate between two regions whereas background noise is inversely related to the ability to differentiate between two regions. Therefore, we picked CNR as one of the parameters for quantifying the imaging performance of SFM. Furthermore, it is pertinent to mention that CNR has a limitation in that it is a display-dependent parameter and therefore, we also measured signal difference to noise ratio (SDNR) for each captured image as it is a display-independent feature.^{24–27}

As a first step, ImageJ was used to manually measure the SDNR and CNR for the captured images.²¹ As mentioned in the materials section and our previous studies, with ImageJ, SDNR and CNR values for one complete image were calculated by calculating SDNR and CNR for ten fluorescent beads in an image and taking their mean.²¹ Evidently, this is a very resource and time-intensive method and it is also prone to manual processing errors. Furthermore, it only gives us an estimate for the true SDNR and CNR of a captured image but not the exact value since we only measure ten beads whereas most captured images contain a lot more than just ten beads. Therefore, it is necessary to come up with an automated algorithm that can calculate the SDNR and CNR parameters for a captured image without being prone to the limitations of manually calculating SDNR and CNR using ImageJ.

Automated quality assessment of fluorescent images (AQAFI) was thus designed to address these limitations by offering researchers an automated way of quantitatively assessing image quality. In image space, the features carry the principal information regarding the pattern or content in the image. In image processing and computer vision, the features in an image are classified into four different types edges, corners, blobs, and ridges. The edges define the boundary between two regions in the image, corners are point-like features, blobs contain information about a region in the image and ridges can be thought of as a generalization of the medial axis in the image. We picked corners to be the salient features in the SFM-captured images and used the fast feature-detection algorithm as explained previously. The higher levels of repeatability and expeditious detection of features³⁰ make fast feature-detection faster and more favorable than its counterparts like HARRIS, Shi-Thomas, DoG, and SUSAN. Since the number of features detected increases with an increase in the total number of beads in an image as seen from ESI Fig. S2–S4,[†] therefore, a feature detection algorithm with low computational costs was required and hence, fast feature detection was the more prudent choice.

Associating the correct set of features after applying a feature detection algorithm with a bead is a crucial task as it is the basis of the remaining processes. After the successful detection of the features as shown in ESI Fig. S2,[†] the feature association is just a simple application of clustering. We employed a technique similar to hierarchical agglomerative clustering to find the location of a bead. The advantage of using hierarchical clustering over other clustering techniques *e.g.* *k*-means is that it does not require predefined cluster centers and can be stopped at any arbitrary number of clusters.

As we assume that the number of beads is unknown in an image *k*-means clustering can not be used. Agglomerative clustering is a bottom-up approach that considers each feature a potential bead or cluster and then re-groups all the beads that have an Euclidean distance less than a predefined threshold d_c . The threshold metrics were empirically selected for different bead sizes and are shown in ESI Table S2.[†]

We assume that a bead in image space has a circular shape with a radius defined as α . The bead intensity can be modeled as the Gaussian distribution with high-intensity pixels located at the center of the bead. As the bead association step might not provide the exact center of the bead, finding the accurate bead intensity becomes a difficult task. To avoid an inaccurate measurement of bead intensity we empirically select a square box of half-length s surrounding the center point of the bead. Afterward, we take the mean of the pixel intensities that are above or equal to the 99th percentile of the total pixel intensities. Selecting 99 percentile values removes the low-intensity pixels that could be associated with the background noise or the vicinity noise and improves the overall estimate of the bead intensity. Selecting a box around the bead is computationally inexpensive as it is a simple case of array slicing as compared to selecting an arbitrary shape where each pixel location is selected separately.

Once the bead intensity and the location of the bead are known the bead pixels in the selected box are removed. However, there remains a possibility of residual pixels from the actual bead due to a slight error in the location estimate of the bead as depicted in ESI Fig. S3.[†] Using these pixels in the actual estimate of the vicinity noise might introduce a constant error. Since the bead intensity is generally orders of magnitude above the vicinity noise, the pixels in the selected box region that have intensity values two standard deviations higher than the mean pixel intensity in the box are discarded. Discarding these pixels helps in making sure that residual higher bead intensity pixels are not included while estimating the bead vicinity noise and thus helps in getting a more accurate estimate of the bead vicinity noise.

Similar to the vicinity noise update process as discussed earlier, the background noise is updated by selecting those pixels that have intensity values one standard deviation below the background noise mean. Since there is a possibility that a bead goes undetected due to no corner being present in the bead as shown in ESI Fig. S3 and S4,[†] If these beads are included in the background noise calculation the overall estimate will be inaccurate. So, we discard high-intensity pixels that have an intensity value greater than one standard deviation as it is empirically observed that background noise has the lowest intensity values and is evenly spread in the image. Using one standard deviation reduces the possibility of selecting high-intensity pixels that could be associated with an undetected bead.

Finally, to improve the accuracy and robustness of the algorithm we apply a similar technique for false positive bead rejection as for the vicinity noise and background noise. Since, the feature detection algorithm uses a difference in intensity value

test, to detect a feature, there lies a possibility that a false feature could be associated with a bead hence leading to a false positive bead in the actual bead detection process. In case the image has a greater background noise, pixels in the background noise could also be classified as beads. The probability of bead pixels having intensity values below two standard deviations of the background noise is very low. So, we select all the beads that have bead intensity greater than the two standard deviations of the background noise and reject the remaining, thereby, improving the overall detected bead count.

Fig. 3 showcases the correlation between the bead intensity obtained for the captured images using manual processing (ImageJ) and the automated algorithm. We can see that there is a good relation between the two for all bead sizes (8.3, 2, 1, 0.8 μm) based on the obtained R^2 values which are all above 0.95. Furthermore, the Bland–Altman plots for the data are also shown in Fig. 3. Taking a closer look at the mean error between the bead intensity values obtained using the algorithm and ImageJ tells us that the automated algorithm on average predicts the bead intensity to be lower compared to ImageJ. This happens because in ImageJ we only consider a small segment of the bead that has the highest fluorescent intensity whereas, in the automated algorithm, we take the mean of more pixels making up the bead which reduces the overall mean fluorescent intensity.

Similarly, Fig. 4 showcases the correlation between the bead vicinity intensity obtained for the captured images using manual processing (ImageJ) and the automated algorithm. We can see that there is a good relation between the two for all bead sizes (8.3, 2, 1, 0.8 μm) based on the obtained R^2 values which are all above 0.95. Furthermore, the Bland–Altman plots for the data are also shown in Fig. 4. Taking a closer look at the mean error between the bead vicinity intensity values obtained using the algorithm and ImageJ tells us that similar to bead intensity, the automated algorithm also on average predicts the bead vicinity intensity to be lower compared to ImageJ. This happens because in ImageJ we only consider a small segment of the bead vicinity region which has the highest fluorescent intensity whereas in the automated algorithm, we take the mean of almost all the pixels constituting the bead vicinity region which reduces the overall mean bead vicinity intensity.

Fig. 5 showcases the correlation between the background noise obtained for the captured images using manual processing (ImageJ) and the automated algorithm. Again, a good relationship between the two for all bead sizes (8.3, 2, 1, 0.8 μm) is obtained based on the obtained R^2 values which are all above 0.95. Additionally, the Bland–Altman plots for the data are also shown in Fig. 5. Taking a closer look at the mean error between the background noise values obtained using the algorithm and ImageJ is almost zero which points towards the robustness of the algorithm.

SDNR and CNR values were calculated for the bead images captured in their respective optimal excitation region using data from ImageJ and the algorithm as shown in Fig. 6. We

can see that the SDNR and CNR values obtained using ImageJ and the algorithm are more or less similar except for the ones obtained for 8.3 μm and the lower end of 2.0 μm (4.1 V). This difference in the SDNR and CNR values can be attributed to the difference in the vicinity intensity and background noise values for these images obtained through ImageJ and the automated algorithm. Since both SDNR and CNR contain these two in the denominator, slight variances in their values manifest as a much larger change in the SDNR and CNR values. ESI Table S3† showcases the values of bead intensity, vicinity intensity, and background noise obtained for 8.3 μm beads using both ImageJ and the algorithm. We can see that the absolute difference between the background and vicinity noise obtained using the algorithm and ImageJ is very small but still, it manifests as a much larger difference in the final values of SDNR and CNR because of the nature of their formulas which are shown in (1) and (3).

Another important thing to notice is that this difference in SDNR and CNR values obtained using ImageJ and the algorithm is much more evident towards the lower end of the excitation voltage and more or less subsides at the higher values of excitation voltage as evident from the SDNR and CNR values calculated for 1.0 μm , and 0.8 μm as shown in Fig. 6C and D. This is because at higher excitation voltages the absolute values for vicinity intensity and background noise increase and thus the SDNR and CNR values are less susceptible to small variations in the background noise.

Furthermore, it is also important to talk about the error bars on the SDNR and CNR values shown in Fig. 6. These error bars represent the variance in the imaging performance of the SFM between different bead samples imaged at a particular excitation voltage and have nothing to do with the performance of the algorithm. Particularly, the error bars for SDNR and CNR values obtained for the 8.3 μm beads using the algorithm are very large as shown in Fig. 6A. It means that the SFM is not very consistent and robust while working at this excitation voltage. This can also be verified visually from ESI Fig. S5† which showcases the three images captured for 8.3 μm beads using the SFM at an excitation voltage of 3.8 V. We can see the difference in the background noise amongst these three images which manifests itself as a high variation in the SDNR and CNR values obtained for 8.3 μm beads using the SFM at an excitation voltage of 3.8 V. Here, we should also comment on the error bars for the SDNR and CNR values (8.3 μm at 3.8 V) obtained manually using ImageJ which are much smaller in comparison to their algorithm counterparts. This difference between the algorithm and ImageJ can be attributed to manual processing errors while using ImageJ.

In addition to the standard fluorescent beads, we also applied the AQAFI algorithm to the fluorescent images of peripheral blood leukocytes to quantify their quality. As seen in Fig. 7A, the algorithm was able to successfully quantify the fluorescence intensity of the imaged leukocytes and thus an R^2 value of 0.99 was obtained. Similarly, in Fig. 7B, we can see that AQAFI was able to successfully quantify the leukocyte vicinity noise. The numbers obtained using AQAFI were lower

compared to the ones obtained using ImageJ as seen from the Bland–Altman analysis shown in Fig. 7(B)(II). This happens because AQAFI considers the box region around a leukocyte while calculating the vicinity noise whereas, with ImageJ however, we draw a line through the highest noise region. Furthermore, a good correlation was observed between the background noise values obtained using AQAFI and the ones obtained using ImageJ. Similar to leukocyte intensity and leukocyte vicinity noise, the background noise values obtained using AQAFI were on average slightly lower compared to the ones obtained manually using ImageJ.

Fig. 7D and E showcase the leukocyte SDNR and CNR values calculated using both AQAFI and ImageJ. SDNR and CNR values from both ImageJ and AQAFI decrease with an increase in the excitation voltage because of an increase in the background noise and leukocyte vicinity intensity as shown in Fig. S6.† Similar to the trends observed for the beads, the SDNR and CNR values for leukocytes obtained using ImageJ and AQAFI are more or less equal except for the ones obtained at the lower excitation voltages. This happens because both SDNR and CNR have background noise and vicinity intensity in their denominators and slight changes in their absolute values manifest themselves as a much larger change in the overall SDNR and CNR values. This difference subsides as we move towards higher excitation voltages where SDNR and CNR are less susceptible to small variations in noise values. Furthermore, since AQAFI considers the entire particle (bead/leukocyte) and a box region around it while calculating the particle intensity and vicinity intensity, the SDNR and CNR values obtained using AQAFI represent a much more realistic number compared to its manually processed ImageJ counterpart.

The developed algorithm AQAFI offers multiple advantages compared to its manual counterpart ImageJ in terms of ease of use, enhanced automation, and a substantial reduction in processing times. Additionally, perhaps the biggest advantage offered by AQAFI is that it gives us much more accurate performance metrics since it analyzes almost all the imaged beads compared to just a fraction in the case of ImageJ. Still, there are some limitations associated with AQAFI that need to be addressed in the future. The users have to tune the hyperparameters for each image depending on the configuration of the fluorescence microscope used to capture the images. The feature detection algorithm is based on detecting corners and thus it may not work on an image with smoothed corners. Additionally, more advanced feature selection and detection methods should be explored to further enhance the robustness and accuracy of AQAFI.

5. Conclusion

Owing to high precision and low cost, smartphone fluorescence microscopes (SFM) are becoming popular in recent days. Though many advanced designs for these devices are being proposed, the quantitative assessment of the quality of

the fluorescent images captured using SFMs remains a challenge. In this study, we have proposed an algorithm (AQAFI), that can be used for automated quality assessment of the fluorescent images captured using SFMs. The proposed algorithm was used to quantitatively assess the quality of different fluorescent bead and fluorescently tagged human leukocyte images. The performance of the proposed algorithm was also benchmarked against manually obtained values measured using ImageJ and a high correlation was found. Thus, the proposed algorithm (AQAFI) can be used by researchers to quantify and validate the performances of different SFM designs and identify areas of improvement. Furthermore, the proposed algorithm can also be easily translated to work with benchtop fluorescence microscopes for the identification of optimal imaging conditions.

Data availability

Data related to this study will be available upon request based on the funding agencies and Rutgers, The State University of New Jersey policies.

Author contributions

M. A. S. participated in conceptualization, study design, algorithm development, writing the original draft, and preparing figures, and data analysis. M. N. T. participated in the study conceptualization, development, and coding of the algorithm, data analysis, and draft writing and review. U. H. participated in conceptualization, study design, funding acquisition, investigation, project administration, resources, supervision, writing, review, and editing.

Conflicts of interest

Authors declare no conflicts of interest.

Acknowledgements

The authors would like to acknowledge the funding support from National Science Foundation (NSF award numbers: 2002511 and 2315376), and New Jersey Health Foundation grant. Authors also acknowledge support from the Department of Electrical and Computer Engineering, and the Global Health Institute at Rutgers, The State University of New Jersey.

References

- 1 J. W. Lichtman and J.-A. Conchello, Fluorescence microscopy, *Nat. Methods*, 2005, 2, 910–919.
- 2 R. Yuste, Fluorescence Microscopy Today, *Nat. Methods*, 2005, 2, 902–904.

- 3 M. J. Sanderson, I. Smith, I. Parker and M. D. Bootman, Fluorescence Microscopy, *Cold Spring Harb. Protocols*, 2014, **10**, DOI: [10.1101/pdb.top071795](https://doi.org/10.1101/pdb.top071795).
- 4 B. Herman, Fluorescence Microscopy, in *Current Protocols in Cell Biology*, 1998.
- 5 M. Renz, Fluorescence microscopy-A historical and technical perspective: Fluorescence Microscopy, *Cytometry, Part A*, 2013, **83**, 767–779.
- 6 X. Huang, D. Xu, J. Chen, J. Liu, Y. Li, J. Song, X. Ma and J. Guo, Smartphone-based analytical biosensors, *Analyst*, 2018, **143**, 5339–5351.
- 7 A. Roda, E. Michelini, M. Zangheri, M. Di Fusco, D. Calabria and P. Simoni, Smartphone-based biosensors: A critical review and perspectives, *TrAC, Trends Anal. Chem.*, 2016, **79**, 317–325.
- 8 C. Vietz, M. L. Schütte, Q. Wei, L. Richter, B. Lalkens, A. Ozcan, P. Tinnefeld and G. P. Acuna, Benchmarking Smartphone Fluorescence-Based Microscopy with DNA Origami Nanobeads: Reducing the Gap toward Single-Molecule Sensitivity, *ACS Omega*, 2019, **4**, 637–642.
- 9 D. Xu, X. Huang, J. Guo and X. Ma, Automatic smartphone-based microfluidic biosensor system at the point of care, *Biosens. Bioelectron.*, 2018, **110**, 78–88.
- 10 Y. Shan, B. Wang, H. Huang, D. Jian, X. Wu, L. Xue, S. Wang and F. Liu, On-site quantitative Hg^{2+} measurements based on selective and sensitive fluorescence biosensor and miniaturized smartphone fluorescence microscope, *Biosens. Bioelectron.*, 2019, **132**, 238–247.
- 11 S. Chung, L. E. Breshears, A. Gonzales, C. M. Jennings, C. M. Morrison, W. Q. Betancourt, K. A. Reynolds and J.-Y. Yoon, Norovirus detection in water samples at the level of single virus copies per microliter using a smartphone-based fluorescence microscope, *Nat. Protoc.*, 2021, **16**, 1452–1475.
- 12 O. Ormachea, A. Villazón, P. Rodriguez and M. Zimic, A Smartphone-Based Low-Cost Inverted Laser Fluorescence Microscope for Disease Diagnosis, *Biosensors*, 2022, **12**(11), 960, DOI: [10.3390/bios12110960](https://doi.org/10.3390/bios12110960).
- 13 Y. Liu, A. M. Rollins, R. M. Levenson, F. Fereidouni and M. W. Jenkins, Pocket MUSE: an affordable, versatile and high-performance fluorescence microscope using a smartphone, *Commun. Biol.*, 2021, **4**, 334.
- 14 V. Müller, J. M. Sousa, H. Ceylan Koydemir, M. Veli, D. Tseng, L. Cerqueira, A. Ozcan, N. F. Azevedo and F. Westerlund, Identification of pathogenic bacteria in complex samples using a smartphone based fluorescence microscope, *RSC Adv.*, 2018, **8**, 36493–36502.
- 15 K. Ming, J. Kim, M. J. Biondi, A. Syed, K. Chen, A. Lam, M. Ostrowski, A. Rebbapragada, J. J. Feld and W. C. W. Chan, Integrated Quantum Dot Barcode Smartphone Optical Device for Wireless Multiplexed Diagnosis of Infected Patients, *ACS Nano*, 2015, **9**, 3060–3074.
- 16 Q. Wei, W. Luo, S. Chiang, T. Kappel, C. Mejia, D. Tseng, R. Y. L. Chan, E. Yan, H. Qi, F. Shabbir, H. Ozkan, S. Feng and A. Ozcan, Imaging and Sizing of Single DNA Molecules on a Mobile Phone, *ACS Nano*, 2014, **8**, 12725–12733.
- 17 S. Wang, L. Zheng, G. Cai, N. Liu, M. Liao, Y. Li, X. Zhang and J. Lin, A microfluidic biosensor for online and sensitive detection of *Salmonella typhimurium* using fluorescence labeling and smartphone video processing, *Biosens. Bioelectron.*, 2019, **140**, 111333.
- 18 Y. Sung, F. Campa and W.-C. Shih, Open-source do-it-yourself multi-color fluorescence smartphone microscopy, *Biomed. Opt. Express*, 2017, **8**, 5075–5086.
- 19 M. A. Sami, K. Wagner, P. Parikh and U. Hassan, 2019 *IEEE Healthcare Innovations and Point of Care Technologies (HI-POCT)*, 2019, pp. 119–122.
- 20 M. A. Sami, M. Tayyab, P. Parikh, H. Govindaraju and U. Hassan, A modular microscopic smartphone attachment for imaging and quantification of multiple fluorescent probes using machine learning, *Analyst*, 2021, **146**, 2531–2541.
- 21 M. A. Sami, M. Tayyab and U. Hassan, Excitation modalities for enhanced micro and nanoparticle imaging in a smartphone coupled 3D printed fluorescent microscope, *Lab Chip*, 2022, **22**, 3755–3769.
- 22 H. Govindaraju, M. A. Sami and U. Hassan, 2022 *IEEE Healthcare Innovations and Point of Care Technologies (HI-POCT)*, 2022, pp. 113–116.
- 23 H. Govindaraju, M. A. Sami and U. Hassan, Machine Learning Enabled Leukocyte Quantification Using Smartphone Coupled 3D Printed Microfluidic Biosensor, *IEEE Access*, 2022, **10**, 85755–85763.
- 24 N. G. Campeau, C. D. Johnson, J. P. Felmlee, J. N. Rydberg, R. K. Butts, R. L. Ehman and S. J. Riederer, MR imaging of the abdomen with a phased-array multicore: prospective clinical evaluation, *Radiology*, 1995, **195**, 769–776.
- 25 B. Siewert, M. R. Patel, M. F. Mueller, J. Gaa, D. G. Darby, C. M. Poser, P. A. Wielopolski, R. R. Edelman and S. Warach, Brain lesions in patients with multiple sclerosis: detection with echo-planar imaging, *Radiology*, 1995, **196**, 765–771.
- 26 S. D. Wolff and R. S. Balaban, Assessing contrast on MR images, *Radiology*, 1997, **202**, 25–29.
- 27 M. K. Adamis, W. Li, P. A. Wielopolski, D. Kim, E. J. Sax, K. C. Kent and R. R. Edelman, Dynamic contrast-enhanced subtraction MR angiography of the lower extremities: initial evaluation with a multisection two-dimensional time-of-flight sequence, *Radiology*, 1995, **196**, 689–695.
- 28 M. A. Sami, Ph.D. thesis, Rutgers The State University of New Jersey, School of Graduate Studies, 2023.
- 29 K. Wagner, M. A. Sami, C. Norton, J. McCoy and U. Hassan, Profiling single-cell level phagocytic activity distribution with blood lactate levels, *RSC Adv.*, 2021, **11**, 21315–21322.
- 30 E. Rosten and T. Drummond, *Computer Vision – ECCV 2006*, Berlin, Heidelberg, 2006, pp. 430–443.